Supporting Information for

BMINN: Learning chemical potentials and parameters from voltage data for multi-phase battery modeling

S1. Experimental

Half battery cells were assembled using EL-CELL™ PAT-Cell with lithium metal foil negative electrodes and synthetic graphite positive electrodes supplied by Customcells Itzehoe GmbH. Although graphite typically serves as an anode in lithium-ion full cells, it functions as a cathode in the half-cell setup due to its positive standard voltage vs. Li/Li+. By convention, we refer to the lithiation of the graphite electrode as "charge" and de-lithiation as "discharge", corresponding to a full-cell setup.

The surface morphology of the secondary graphite particles was examined using a scanning electron microscope (FEI Quanta 200 FEG). The electrode samples were prepared by placing the graphite particles onto an adhesive tape to lock them in place for imaging. The SEM image in Fig.2a of the main text was acquired at an accelerating voltage of 10 kV, with various magnifications used to capture detailed particle morphology.

For the assembly, the electrode sheets were die-cut into 18 mm diameter coin-sized discs. A thick Borosilicate glass fiber separator (260 µm, Whatman FG/A) was used to prevent micro internal short circuits. A cutoff voltage of 0 V was chosen for charging to avoid lithium plating on the graphite particles, while for discharging, the cutoff voltage was set to 3 V to prevent over-discharging. A 90 µL solution of lithium hexafluorophosphate in a mixture of ethylene carbonate and dimethyl carbonate ($LiPF_6$ LP50) was used as the electrolyte. Lastly, a formation cycle was performed following the guidelines provided by Customcells, resulting in a nominal capacity of 7.5 mAh at 0.195 mA discharge, which was used as the basis to define C-rates.

Experiments were carried out on PAT-Stand-1 cell holders in a thermal chamber maintained at a constant temperature of 25 °C. After the formation cycle, galvanostatic charge-discharge cycles at C/20 and C/40 were conducted on a NEWARE™ coin cell tester, with a resting time of 5 h between charge and discharge cycles. The current and voltage data were collected at a sampling frequency of 1 Hz. The normalized capacity of the assembled half-cells was calculated from charge/discharge capacity using a linear relationship determined by two dQ/dV peaks centering at normalized capacity values 1/12 and 1/2. This conversion was employed to normalize the capacity measurements so that the voltages, e.g., 0.203 V and 0.074 V under C/20 charge, align with the two critical stoichiometries marking the end of two known phase transitions [1].

Fig. 1 shows the charge-discharge curves for the half-cell setup. It is evident that there is a capacity difference between charge and discharge due to Coulombic efficiency. In this study, we consider only the intercalation reaction; the data used for physics-based learning should exclude all side reactions. To achieve this, we assume a 100% Faraday efficiency for the desired electrochemical reaction, i.e., intercalation reaction, and scale the discharge capacity to compensate for the loss due to side reactions. The scaled voltage curves are plotted in green in Fig. 1.

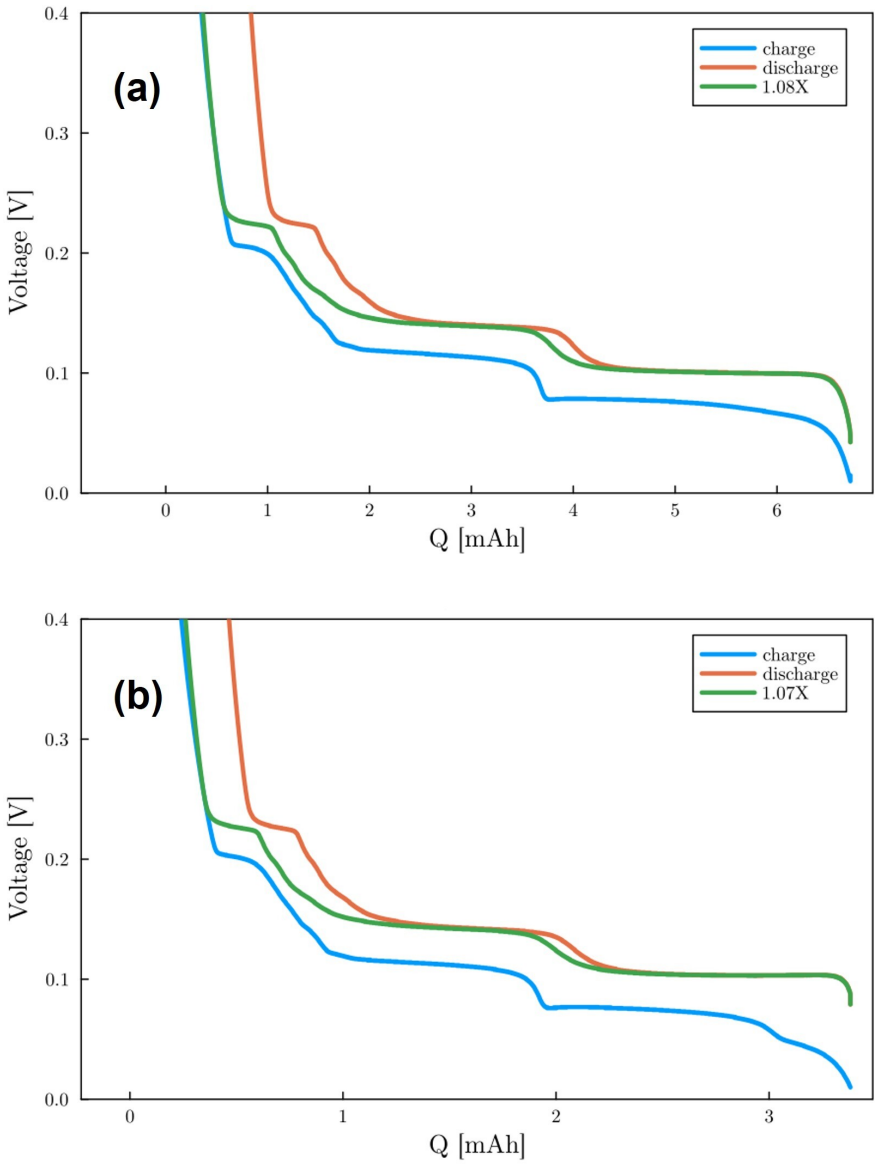

Figure 1: Charge-discharge curves with scaled discharge capacities (green curves) assuming a 100% Faraday efficiency. The C-rates used for the cycling are (a) C/40 and (b) C/20.

S2. Diffusion-limited intercalation

In physics-based learning, two key components are involved: a fixed model structure, derived from a physics-based formulation, and an approximator with tunable parameters. In the study, we utilize two physics-based formulations corresponding to two equally infeasible physical scenarios discussed in the main text.

Secondary graphite particles can be modeled by either solid-solution particles as in the DFN model [2] or by phase-separating particles in the phase-field model [3–5], with varying modeling errors. This section adapts the general formulation of the phase-field model to suit the modeling of material-specific phase separation within secondary graphite particles. Under diffusion limitation, the dynamics of the solid-phase lithium-ion concentration $C_s(r,t)$ at a distance r from the center of a spherical, secondary graphite particle at time t, can be modeled by the Cahn-Hilliard

equation

$$r^2 \frac{\partial C_s}{\partial t} = \frac{\partial}{\partial r}\left(\frac{D_s}{k_B T} C_s r^2 \frac{\partial \mu}{\partial r}\right), \tag{1}$$

where $D_s(C_s)$ is the concentration-dependent diffusion coefficient, and k_B is the Boltzmann constant. The chemical potential μ is further denoted by μ_{pf} and μ_{pe} for the phase-field model [6] and in porous electrode theory (PET) based model [7], respectively. Specifically, μ_{pf} and μ_{pe} are mathematically defined as

$$\mu_{\text{pf}} = e_0 \phi_{\text{ref}} + \mu_{\text{pf}}^h(C_s) - \frac{\kappa}{C_{\max}^2}\left(\frac{2}{r}\frac{\partial C_s}{\partial r} + \frac{\partial^2 C_s}{\partial r^2}\right) \quad \text{(phase-field model)}, \tag{2a}$$

$$\mu_{\text{pe}} = k_B T \ln \frac{C_s}{C_{\max}} \quad \text{(PET-based model)}, \tag{2b}$$

where e_0 denotes the elementary charge, and ϕ_{ref} is a reference potential defined by a fixed potential plateau. The second term $\mu_{\text{pf}}^h(C_s)$ in (2a) represents the homogeneous part of the chemical potential, which is a function of the concentration C_s. $C_{\max}$ and κ are the maximum lithium-ion site density in graphite and the gradient energy coefficient for a diffuse phase boundary. Importantly, $\mu_{\text{pe}}(C_s)$ is strictly monotonic in C_s (since $\partial \mu_{\text{pe}}/\partial > 0$), which corresponds to a convex homogeneous free energy. As a result, this PET-based model cannot generate miscibility gaps, metastable branches, or free-energy barriers, and therefore cannot represent phase separation and staging transitions. By contrast, in the phase-field formulation $\mu_{\text{pf}}(C_s)$, the chemical potential contains a homogeneous term and a gradient term that together enable non-convex free energies.

In the phase-field model, the (homogeneous) Gibbs free energy $\mathcal{G}_{\text{pf}}$ is an integral defined by

$$\mathcal{G}_{\text{pf}} = \int_0^{C_{\max}} \left(\mu_{\text{pf}}^h(C_s) - e_0 \phi_{\text{ref}}\right) dC_s. \tag{3}$$

Existing phase-field models for graphite [3–5] assume that μ_{pf}^h in (2a) can be directly calculated from OCP, ϕ_{OCP}, by the relation

$$\mu_{\text{pf}}^h = e_0 \phi_{\text{OCP}} - e_0 \phi_{\text{ref}}. \tag{4}$$

where ϕ_{OCP} is a function of $C_s/C_{\max}$. However, this relation is only true for solid-solution materials. For phase-separating materials such as graphite, ϕ_{OCP} does not follow the trajectory of the chemical potential but rather the common tangents [8]. Different from this approach of adopting a function μ_{pf}^h using OCP, we consider that the function is unknown *a priori* for the phase-field model.

To finish the formulation, four boundary conditions arise for the particle-level intercalation with a boundary flux defined by $\mathcal{J} = -(D_s/k_B T)\, C_s\, \partial \mu/\partial r$ at the boundary given by

$$\left.\frac{\partial C_s}{\partial r}\right|_{r=0} = 0, \qquad \left.\mathcal{J}\right|_{r=0} = 0, \tag{5}$$

$$\left.\frac{\kappa}{C_{\max}^2}\frac{\partial C_s}{\partial r}\right|_{r=R} = \frac{\partial \gamma_s}{\partial C_s}, \qquad \left.\mathcal{J}\right|_{r=R} = j, \tag{6}$$

where γ_s is the surface energy that controls surface wetting, R is the secondary particle's radius, and j is the intercalation rate. In the above equations, (5) is imposed to satisfy the spherical symmetry in particles and the no-flux condition at the center of particles, and (6) is due to surface wetting and the intercalation current at the particle surface. The surface wetting can be phenomenologically attributed to graphene layers exposed on the surface acting as a highway

for intercalation [9]. The intercalation current j can be modeled by a symmetric Butler-Volmer equation [7]

$$j = \frac{2\,k_0\,j_0}{\mathcal{F}}\,\sinh\left(\frac{e_0}{2k_BT}\,\eta\right), \tag{7}$$

where k_0, η, k_B, $\mathcal{F}$ and T are the exchange current density, overpotential, Boltzmann constant, Faraday constant and temperature, respectively. j_0 is the exchange current and takes the form $j_0 = \mathcal{F}\sqrt{C_e C_s^R (C_{\max} - C_s^R)}$, where C_e is the electrolyte concentration treated as a constant in this work in accordance with the single-particle assumption, and $C_{\mathrm{s}}^{\mathrm{R}}$ is the surface concentration.

For the phase-field model described by (1), (2a), and (5)–(7), the voltage of the graphite electrode, denoted by V_{pf}, can be calculated as

$$V_{\mathrm{pf}}(t) = -\frac{1}{e_0}\mu_{\mathrm{pf}}^h\left(C_s^R(t)\right) + \eta(t) - \frac{R_{\mathrm{c}}}{A_{\mathrm{s}}}I(t), \tag{8}$$

where I represents the applied current, R_{c} accounts for the polarization in the voltage due to contact resistance, and A_{s} is the electrode surface area. Similarly, the graphite electrode's voltage in the PET-based model consisting of (1), (2b), and (5)–(7) is given by

$$V_{\mathrm{pet}}(t) = \phi_{\mathrm{OCP}}\left(C_s^R(t)\right) + \eta(t) - \frac{R_{\mathrm{c}}}{A_{\mathrm{s}}}I(t), \tag{9}$$

where ϕ_{OCP} represents the OCP and is a function of C_s^R.

S3. Reaction-limited intercalation

In battery systems, the overpotential drives the kinetic processes taking place on the electrolyte-particle interface due to an imbalance between the chemical potential at the interface and that inside of a particle. The diffusion-limited picture described in Section S2 considers the phase separation or migration of interfaces within the secondary particles. This section develops a physics-based model for reaction-limited phase separation driven by the chemical potential difference in the ensemble of primary graphite particles. Under reaction limitation, the chemical potential gradient inside primary particles is negligible. The driving force for electrochemical reactions is solely due to the difference between the chemical potential of primary particles μ_i and the chemical potential of their ensemble, i.e., the reservoir chemical potential μ_{res}. Hence, the concentration of these primary particles can be modeled as a function of time only and is expressed as $C_i(t)$ for particle i.

For a single primary graphite particle in Fig. 1c of the main text, the dynamics of particle concentration C_i is a stochastic filling process governed by the Langevin equation [10, 11]

$$\frac{dC_i(t)}{dt} = a_i J_i(t) + \Gamma(t), \tag{10}$$

where a_i is the volumetric surface area of the particle. Γ is a random noise due to thermal fluctuations, and we assume that it is not dependent on the intercalation rate J_i of particle i but on temperature alone.

Different from Butler-Volmer kinetics, which is known to yield inaccurate results at high overpotential, we assume the coupled ion-electron transfer kinetics [12] for J_i, leading to

$$J_i = i_0 \cdot (1 - \tilde{c}_i) \cdot \sqrt{\pi\tilde{\lambda}} \cdot \left(\frac{\tilde{c}_e}{1 + \exp(\tilde{\eta}_\rho)} - \frac{\tilde{c}_i}{1 + \exp(-\tilde{\eta}_\rho)}\right) \cdot \mathrm{erfc}\left(\frac{\tilde{\lambda} - \sqrt{1 + \sqrt{\tilde{\lambda}} + \tilde{\eta}_\rho^2}}{2\sqrt{\tilde{\lambda}}}\right), \tag{11}$$

where $\tilde{c}_i$ represents a normalized concentration defined as $\tilde{c}_i = C_i/C_{\max}$, erfc$(\cdot)$ is the complementary error function, i_0 is the intercalation rate constant, $\tilde{c}_e$ is the normalized electrolyte concentration, and $\tilde{\lambda}$ is the Marcus reorganization energy scaled to k_BT. The formal overpotential $\tilde{\eta}_\rho$, scaled to thermal voltage k_BT/e_0, is defined as

$$\tilde{\eta}_\rho = (\mu_{\text{res}} - \mu_{\text{rl}})/k_BT + \ln(\tilde{c}_e/\tilde{c}_i), \tag{12}$$

in which the ensemble chemical potential μ_{res} is an algebraic variable, and μ_{rl} is the graphite chemical potential of the reaction-limited model.

Owing to charge conservation, the total intercalation rate is constrained by the applied current I. By assuming all primary particles with the same volume and surface area, i.e. $a_i = a_s$ for any particle i, this constraint can be formulated as

$$e_0 a_s A_s \sum_{i=1}^{N_p} J_i = I\,, \tag{13}$$

where N_p represents the total number of primary graphite particles.

Eqns. (10)–(13) form a system of stochastic differential-algebraic equations (SDAEs). It is well known that as N_p approaches infinity, the SDAE system is equivalent to the Fokker-Planck equation, with a stochastic process $\tilde{c}$ that admits a population density $\rho(t, \tilde{c})$, which is given by

$$\frac{\partial \rho}{\partial t} + \frac{a_s}{C_{\max}} \frac{\partial \rho J}{\partial \tilde{c}} = \nu \frac{\partial^2 \rho}{\partial \tilde{c}^2}, \tag{14}$$

where ν denotes the thermal diffusivity, $\tilde{c}$ indicates the ensemble concentration of primary particles, and J signifies the reaction-limited intercalation rate of the ensemble.

Eqn. (14) is subject to a constraint due to the total applied current (13). Substituting (10) into (13) and considering the continuous concentration $\tilde{c}$ with its associated density ρ, we can derive

$$e_0 C_{\max} V_{\text{a}} \frac{d}{dt} \int_0^1 \tilde{c}\rho d\tilde{c} = I, \tag{15}$$

where V_{a} denotes the volume of active materials. Given that there is no flux at $\tilde{c} = 0$ and $\tilde{c} = 1$, the following boundary conditions apply:

$$\left(\nu \frac{\partial \rho}{\partial \tilde{c}} - \frac{a_s}{C_{\max}} \rho J \right) \Bigg|_{\tilde{c}=0,1} = 0. \tag{16}$$

Similar to Section S2, we assume the material-specific chemical potential μ_{rl} of an unknown form for the reaction-limited model. The Gibbs free energy in the reaction-limited model $\mathcal{G}_{\text{rl}}$ can then be calculated by the integral

$$\mathcal{G}_{\text{rl}} = \int_0^1 \mu_{\text{rl}}(\tilde{c}) - e_0 \phi_{\text{ref}}\, d\tilde{c}. \tag{17}$$

Finally, in the reaction-limited battery model governed by (11)–(12), (14)–(16), the voltage of the graphite electrode, V_{rl}, can be calculated by

$$V_{\text{rl}}(t) = -\frac{\mu_{\text{res}}(t)}{e_0} - \frac{R_{\text{c}}}{A_{\text{s}}} I(t). \tag{18}$$

S4. Dimensionless equations

The equations in Section S2 and Section S3 feature physically meaningful parameters with widely varying numerical values, spanning tens of orders of magnitude. Although the physics-based battery models contain many parameters, BMINN does not infer all constants independently from voltage data. Instead, we infer only a reduced set of identifiable parameter groups. Parameter learning is performed in a Bayesian manner, yielding posterior distributions that quantify identifiability and uncertainty.

S4.1 Assumption

By single-particle assumption for small current rate, the intercalation rate j can be treated as a constant across the electrode thickness dimension, namely $j = I/(a_s \mathcal{F} A_s \delta_a)$. Here, δ_a is the anode thickness, and $a_s = 3\epsilon_s/R$ is the specific interfacial area in which the volume fraction of active material is denoted by ϵ_s. Based on these definitions and calculations, as the output of the two battery models, the predicted electrode voltage represented in (8)–(9) and (18) become

$$V_{\text{pf}} = -\frac{1}{e_0}\mu^h_{\text{pf}}\left(C^R_s/C_{\max}\right) - \frac{2k_BT}{e_0}\sinh^{-1}\left(\frac{I}{2a_s\mathcal{F}A_s\delta_a k_0 j_0}\right) - \frac{R_c}{A_s}I, \tag{19}$$

$$V_{\text{pe}} = \phi_{\text{OCP}} - \frac{2k_BT}{e_0}\sinh^{-1}\left(\frac{I}{2a_s\mathcal{F}A_s\delta_a k_0 j_0}\right) - \frac{R_c}{A_s}I, \tag{20}$$

$$V_{\text{rl}} = -\frac{\mu_{\text{res}}}{e_0} - \frac{R_c}{A_s}I. \tag{21}$$

It is worth noting that within the PET-based model, (20) is deterministic for producing the electrode voltage. For this model, the task of BMINN is to learn the physical parameters from noisy data.

S4.2 Diffusion-limited intercalation

To follow conventions, we first scale the concentrations and radius by their respective maximum values, i.e. $\tilde{c} = C_s/C_{\max}$ and $\tilde{r} = r/R$. Note that we do not scale time as the measured voltage data constitutes a time series measured in seconds. Preserving the original time scale ensures consistency in parameter estimation. For PET-based model we consider a constant diffusivity $D_s(\tilde{c}) = D_0$, and for the phase field model, we adopt a diffusivity that takes account of excluded sites, $D_s = D_0(1-\tilde{c})$. Consequently, equation (1) becomes

$$\tilde{r}^2\frac{\partial\tilde{c}}{\partial t} = \frac{D_0}{R^2}\frac{\partial}{\partial\tilde{r}}\left((1-\tilde{c})\tilde{c}\,\tilde{r}^2\frac{\partial\tilde{\mu}}{\partial\tilde{r}}\right).$$

Considering a constant intercalation rate $j = I/(a_s A_s \delta_a)$, where $a_s = 3\epsilon_s/R$. The boundary conditions then take the form

$$\left.\frac{\partial\tilde{c}}{\partial\tilde{r}}\right|_{\tilde{r}=0} = 0, \qquad \left.\tilde{F}\right|_{\tilde{r}=0} = 0,$$

$$\left.\frac{\partial\tilde{c}}{\partial\tilde{r}}\right|_{\tilde{r}=1} = \frac{R}{\kappa}\frac{\partial\gamma_s}{\partial\tilde{c}}, \qquad \left.\tilde{F}\right|_{\tilde{r}=1} = \frac{R^2}{D_0}\frac{I}{3\epsilon_s C_{\max}\mathcal{F}A_s\delta_a},$$

where $\tilde{F} = -D_0(1-\tilde{c})\tilde{c}\,\partial\tilde{\mu}/\partial\tilde{r}$ for the phase field model and $\tilde{F} = -D_0\tilde{c}\,\partial\tilde{\mu}/\partial\tilde{r}$ for PET-based model. Next, we scale the chemical potential by thermal voltage, i.e. $\tilde{\mu} = \mu/k_BT$,

$$\begin{aligned}
\tilde{\mu}_{\mathrm{pf}} &= \frac{e_0}{k_BT}\cdot\phi_{\mathrm{ref}} + \frac{\mu^h_{\mathrm{pf}}(\tilde{c})}{k_BT} - \frac{\kappa}{C_{\max}R^2k_BT}\left(\frac{2}{\tilde{r}}\frac{\partial\tilde{c}}{\partial\tilde{r}} + \frac{\partial^2\tilde{c}}{\partial\tilde{r}^2}\right) \quad \text{(phase-field model)},\\
\tilde{\mu}_{\mathrm{pe}} &= \ln\tilde{c} \quad \text{(PET-based model)},
\end{aligned}$$

and similarly, for the output functions, we scale the surface concentration by maximum site density

$$\begin{aligned}
V_{\mathrm{pf}}(t) &= -\frac{1}{e_0}\mu^h_{\mathrm{pf}}\left(\tilde{c}^R(t)\right) - \frac{2k_BT}{e_0}\sinh^{-1}\left(\frac{1}{3\epsilon_sC_{\max}\mathcal{F}A_{\mathrm{s}}\delta_{\mathrm{a}}}\frac{R}{2k_0\sqrt{C_e}}\frac{I}{\sqrt{\tilde{c}^R(1-\tilde{c}^R)}}\right) - \frac{R_{\mathrm{c}}}{A_{\mathrm{s}}}\cdot I(t),\\
V_{\mathrm{pe}}(t) &= \phi_{\mathrm{OCP}}\left(\tilde{c}^R(t)\right) - \frac{2k_BT}{e_0}\sinh^{-1}\left(\frac{1}{3\epsilon_sC_{\max}\mathcal{F}A_{\mathrm{s}}\delta_{\mathrm{a}}}\frac{R}{2k_0\sqrt{C_e}}\frac{I}{\sqrt{\tilde{c}^R(1-\tilde{c}^R)}}\right) - \frac{R_{\mathrm{c}}}{A_{\mathrm{s}}}\cdot I(t).
\end{aligned}$$

Notice that there exists a minimum number of parameter groups, 6 for the phase field model and 4 for the PET-based model. We list them as follows, where

$$\begin{aligned}
\theta_1 &= \frac{R^2}{D_0},\\
\theta_2 &= \epsilon_sC_{\max}\mathcal{F}A_{\mathrm{s}}\delta_{\mathrm{a}},\\
\theta_3 &= \frac{R}{2k_0\sqrt{C_e}},\\
\theta_4 &= \frac{R_{\mathrm{c}}}{A_{\mathrm{s}}},\\
\theta_5 &= \frac{\kappa}{C_{\max}R^2k_BT},\\
\theta_6 &= \frac{RC_{\max}}{\kappa}\frac{\partial\gamma_s}{\partial C_s}.
\end{aligned}$$

To conclude, the reformulated equations to be solved alone with the inferred parameter groups are

$$\begin{cases}
\theta_1\tilde{r}^2\frac{\partial\tilde{c}}{\partial t} = \frac{\partial}{\partial\tilde{r}}\left((1-\tilde{c})\tilde{c}\,\tilde{r}^2\frac{\partial\tilde{\mu}}{\partial\tilde{r}}\right)\\
\left.\frac{\partial\tilde{c}}{\partial\tilde{r}}\right|_{\tilde{r}=0} = 0 \qquad \left.\tilde{F}\right|_{\tilde{r}=0} = 0\\
\left.\frac{\partial\tilde{c}}{\partial\tilde{r}}\right|_{\tilde{r}=1} = \theta_6, \qquad \left.\tilde{F}\right|_{\tilde{r}=1} = \frac{I\theta_1}{3\theta_2}\\
\tilde{\mu}_{\mathrm{pf}} = \frac{e_0}{k_BT}\cdot\phi_{\mathrm{ref}} + \mu^h_{\mathrm{pf}} - \theta_5\left(\frac{2}{\tilde{r}}\frac{\partial\tilde{c}}{\partial\tilde{r}} + \frac{\partial^2\tilde{c}}{\partial\tilde{r}^2}\right) \quad \text{(phase-field model)}\\
\tilde{\mu}_{\mathrm{pet}} = \ln\tilde{c} \quad \text{(PET-based model)}\\
V_{\mathrm{pf}}(t) = -\frac{k_BT}{e_0}\mu^h_{\mathrm{pf}}\left(\tilde{c}^R(t)\right) - \frac{2k_BT}{e_0}\sinh^{-1}\left(\frac{\theta_3}{3\theta_2}\frac{I}{\sqrt{\tilde{c}^R(1-\tilde{c}^R)}}\right) - \theta_4\cdot I(t)\\
V_{\mathrm{pet}}(t) = \phi_{\mathrm{OCP}}\left(\tilde{c}^R(t)\right) - \frac{2k_BT}{e_0}\sinh^{-1}\left(\frac{\theta_3}{3\theta_2}\frac{I}{\sqrt{\tilde{c}^R(1-\tilde{c}^R)}}\right) - \theta_4\cdot I(t)
\end{cases}$$

Using approximate Bayesian computation, the six grouped parameters for the phase-field model are identified, and their posterior distributions are shown in a correlation plot in Fig. 2. Since the posterior distributions exhibit approximately a unimodal pattern, we conclude that all the grouped physical parameters are identifiable given the input and output data.

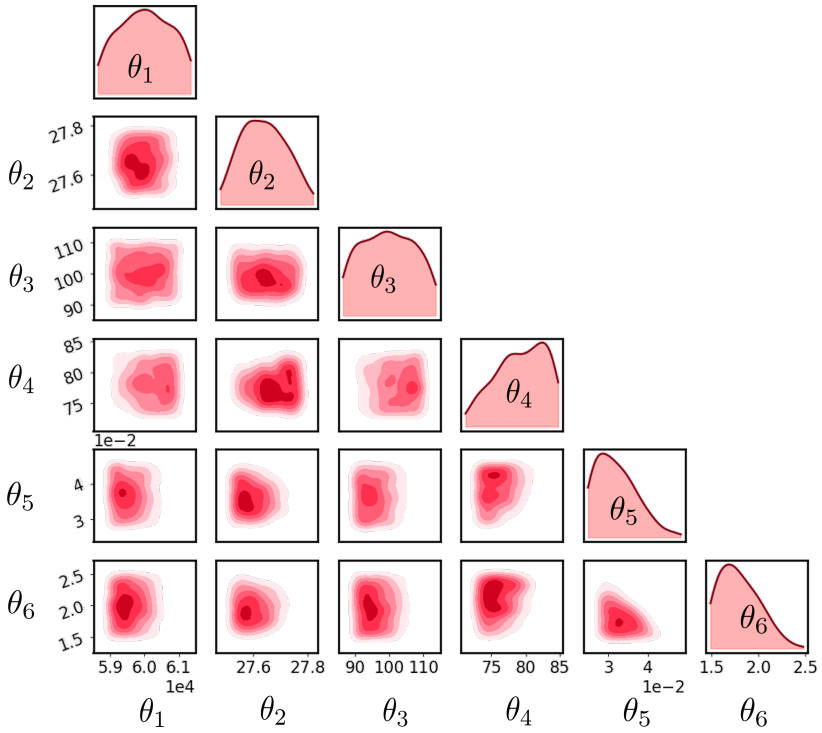

Figure 2: Posterior distribution of the physical parameters of the phase field model.

S4.3 Reaction-limited intercalation

Similarly, for the reaction-limited model described in section S3, there exist four groups of parameters,

$$\theta_7 = \frac{a_s i_0}{C_{\max}},$$
$$\theta_8 = \nu,$$
$$\theta_9 = e_0 C_{\max} V_a,$$
$$\theta_{10} = \frac{R_c}{A_s}.$$

The inherent physical significance of these parameters can be described as follows: $1/\theta_7$, in units of second, is the relaxation time of particles. θ_8 is related to the width of population density peaks, characterizing how widely the distribution is spread around a mean stoichiometry. This is controlled by the thermal diffusivity, which is temperature dependent. In this work, we consider the isothermal condition, and therefore θ_8 is a constant. Meanwhile, θ_9 determines the nominal capacity, which can not be measured precisely experimental but is identified through parameter estimation. Lastly, θ_{10} measures the contact resistance per unit surface area, contributing to a current-dependent voltage drop/rise during charging/discharging. Incorporating the parameter groupings, the reaction-limited model can be

reformulated as

$$
\begin{cases}
\frac{\partial \rho}{\partial t} + \theta_7 \frac{\partial(\rho \circ J)}{\partial \tilde{c}} = \theta_8 \frac{\partial^2 \rho}{\partial \tilde{c}^2} \\
\theta_9 \frac{d}{dt} \int_0^1 \tilde{c} \rho d\tilde{c} = I \\
\left(\theta_8 \frac{\partial \rho}{\partial \tilde{c}} - \theta_7 \rho \circ J\right)\Big|_{\tilde{c}=0,1} = 0 \\
J = (1-\tilde{c}) \cdot \sqrt{\pi \tilde{\lambda}} \cdot \left(\frac{\tilde{c}_e}{1+\exp(\tilde{\eta}_\rho)} - \frac{\tilde{c}}{1+\exp(-\tilde{\eta}_\rho)}\right) \cdot \operatorname{erfc}\left(\frac{\tilde{\lambda} - \sqrt{1+\sqrt{\tilde{\lambda}}+\tilde{\eta}_\rho^2}}{2\sqrt{\tilde{\lambda}}}\right) \\
\tilde{\eta}_\rho = (\mu_{\text{res}} - \mu_{\text{rl}})/k_B T + \ln(\tilde{c}_e/\tilde{c}) \\
V_{\text{rl}}(t) = -\frac{\mu_{\text{res}}(t)}{e_0} - \theta_{10} \cdot I(t)
\end{cases}
$$

S5. Half cell voltage

The chemical potentials μ_{pf}^h and μ_{rl}, learned from the C/40 charge-discharge dataset were validated against experimentally measured voltage data under C/20 and C/5 testing currents. In Fig. 3, three distinct voltage plateaus and their transitions are evident on C/20 charge and discharge curves. The blue and red solid curves represent the model predictions of electrode voltage defined in (19) and (21), sampled from the posterior distribution of parameters. It can be seen that both models closely follow the experimental voltage measurements (dashed curves), although the reaction-limited model in Fig. 3b is less accurate at high capacity towards the end of charge. This portion of the capacity is usually unused in full cells since the cathode potential often increases sharply, reaching the cutoff voltage for charge. However, as the battery undergoes aging, the degradation process will increase the cutoff capacity of the anode due to shifting utilization windows [13]. Hence, the accuracy of anode potential prediction at high capacity is crucial in adaptive aging modeling. For instance, the reaction-limited model overestimates the anode potential during the C/20 charge after 20 hours, as shown in Fig. 3b. Under such circumstances, while the true anode potential is approaching 0 V, the estimated value is still far from it. Consequently, health-aware control algorithms based on this estimated anode potential will lead to unexpected lithium plating and dendritic formation.

For the C/5 testing current, both models in Fig. 3 give root mean square errors (RMSE) of less than 20 mV, compared to the PET-based model of 50 mV. The modeling error for these two models may stem from the fact that local potentials vary in both in-plane and out-of-plane directions and that the single-particle assumption is adopted herein. In out-of-plane direction, the spatial gradients of the intercalation rate are enlarged as the applied current increases. Even though this behavior can be accounted for by considering spatially distributed battery states in the out-of-plane (thickness) direction, it is found that the potential difference is significant in the in-plane direction for commercial cells [14, 15]. X-ray diffraction also confirmed the graphite heterogeneous dynamics in the in-plane direction, which calls for heterogeneous pseudo-3-dimensional modeling [16]. In our coin cell experiments, we have also observed *post-mortem* the in-plane heterogeneous filling even for a small 18 mm electrode (Fig. 4). To resolve this modeling error for battery fast-charging control, a possible simple solution is to subtract the anode potential prediction by an offset voltage, instead of resorting to more complex models. However, this offset value has to be experimentally determined at different conditions, such as state of health and state of charge (SOC) values.

For the C/5 testing current, models that assume constant lithium-ion concentration in the electrolyte and a uniform intercalation rate on the particle surface tend to overestimate the anode potential. As discussed, this modeling error arises not only from the single-particle assumption, which presumes a uniform intercalation rate and overpotential across the thickness dimension (out-of-plane direction), but also from the assumption that these parameters remain constant in the in-plane direction. This limitation is evident in an 18 mm-diameter coin cell, as shown in Fig. 4, where a teardown performed in the glovebox reveals a ring-like heterogeneous distribution of solid concentration after C/5 cycling.

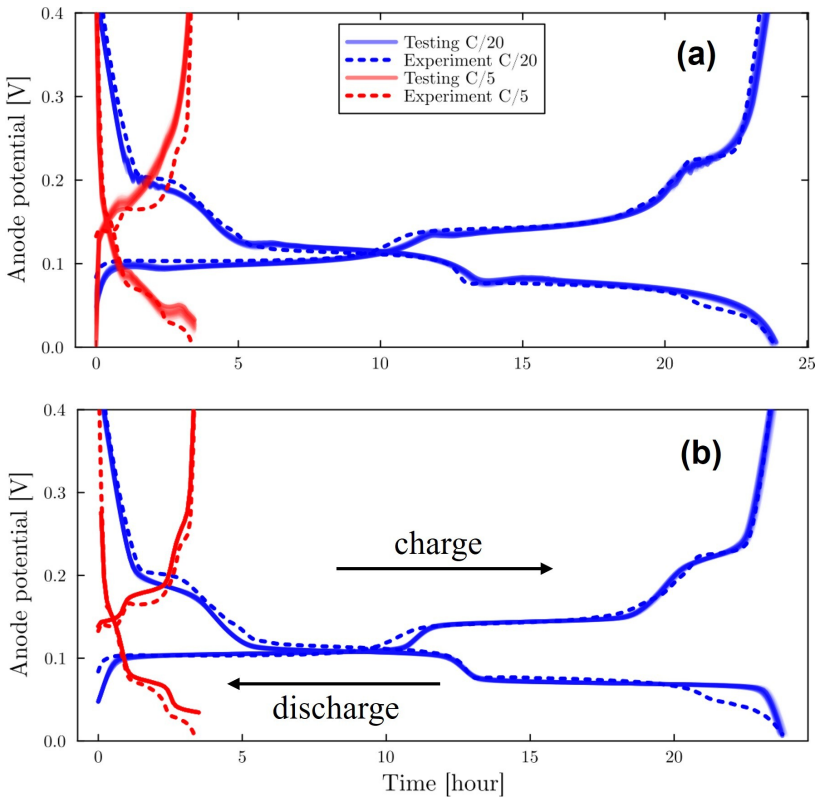

Figure 3: Comparison of measured voltage data (dashed) and model predictions under C/20 and C/5 testing currents obtained by computing 100 predictions using parameters sampled from the posterior of θ_τ. (a) Phase-field model. (b) Reaction-limited model. Darker regions indicate areas of higher probability density.

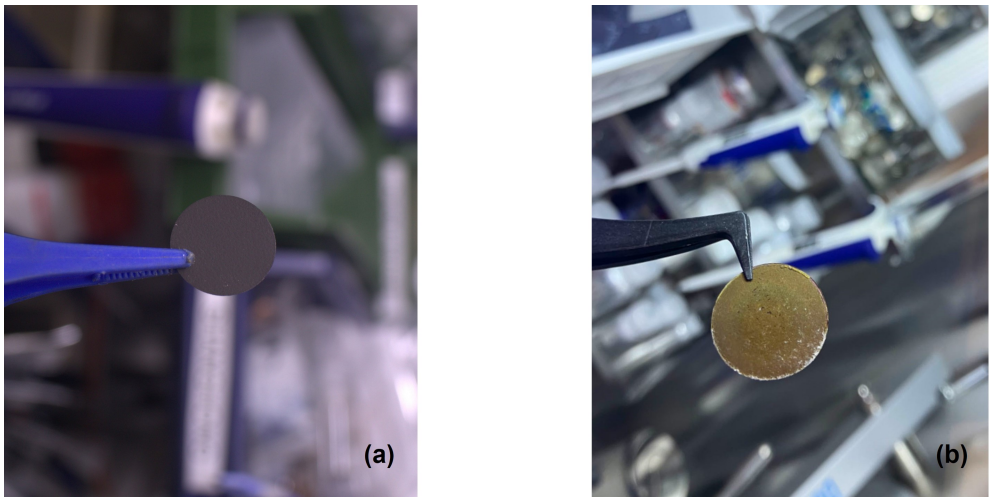

Figure 4: Boundary effect illustrated by in-plane heterogeneous filling of a 18 mm electrode. (a) Pristine graphite electrode before cycling. (b) *Post-mortem* graphite electrode after cycling, which showed ring-like coloring.

This heterogeneity is likely caused by an electrolyte concentration gradient induced by surface wetting at the boundary of the circular electrode. Such boundary effects diminish as the area-to-boundary ratio increases (e.g., in commercial

cells) but are exacerbated under higher current rates.

It is worth noting that in our half-cell experiments, we fixed the temperature to avoid additional uncertainties associated with fitting temperature-dependent parameters, such as the prefactor and activation energy in the Arrhenius expression. Including these parameters would otherwise complicate the training process and introduce further variability, which we aimed to minimize in this study. This is analogous to our decision to use small currents and the single-particle assumption in the learning process. In subsequent downstream applications, such as full-cell modeling under large currents, one needs to relax these assumptions and incorporate additional dynamics to account for electrolyte effects and spatially distributed intercalation rates. Temperature effects can be incorporated by introducing temperature-dependent parameters, which are typically fitted from experimental data collected at different temperatures. In many cases, this involves assuming that certain phenomena are thermally activated (for example, diffusion), with an associated activation energy to be determined. A common approach is to use an Arrhenius-type expression for the fitting.

S6. Conversion from radius-dependent concentration to population density and XRD intensity

The phase-field formulations do not feature population density due to the single-particle assumption. This assumption assumes that the intercalation rate is the same in both electrode in-plane and out-of-plane directions. Therefore, only one single particle is needed to represent the whole particle population. The state of the system is the radius-dependent concentration profile for the single, graphite secondary particle.

In order to cross-validate the XRD data, a conversion is needed from concentration to population density. To do this, we assume that all the secondary particles are of spherical shape and of the same particle size. The former allows easy integration of particle volume, and the latter simplifies the integrals of the whole population to an integral of a single particle. To achieve this, let $\tilde{c}$ be a matrix of size $m \times n$, $\tilde{c}_{\mathrm{rl}}$ be a vector of length l, ϵ_{tol} and $\tilde{r}$ of length m be a vector of radii corresponding to the elements of $\tilde{c}$. $\tilde{c}[\tilde{r}, \tau_{\mathrm{n}}]$ is the concentration field in the phase field model where the matrix form here represents its snapshots. $\tilde{c}_{\mathrm{rl}}$ is the concentration coordinate in the relation-limited model, and n is the number of sampled time τ_{n}. The goal is to compute a matrix $\tilde{\rho}[\tilde{c}_{\mathrm{rl}}, \tau_{\mathrm{n}}]$ representing the snapshots of population density based on the proximity (defined by the tolerance ϵ_{tol}) of values in $\tilde{c}$ to the elements of $\tilde{c}_{\mathrm{rl}}$. This can be done using Algorithm 1 in which $I_{i,j}$ represents the set of indices k where the condition $(\tilde{c}[k, j] - \tilde{c}_{\mathrm{rl}}[i])^2 \leq \epsilon_{\mathrm{tol}}$ is satisfied for the j-th column of $\tilde{c}$.

Algorithm 1: Conversion from $\tilde{c}[\tilde{r}, \tau_{\mathrm{n}}]$ to $\tilde{\rho}[c_{\mathrm{rl}}, \tau_{\mathrm{n}}]$

Input: $\tilde{c}[\tilde{r}, \tau_{\mathrm{n}}]_{m \times n}$, $\tilde{c}_{\mathrm{rl}}$, $\tilde{r}$, $\tilde{c}_{\mathrm{rl}}$ and ϵ_{tol}
Output: $\tilde{\rho}[\tilde{c}_{\mathrm{rl}}, \tau_{\mathrm{n}}]_{l \times n}$
for $j \leftarrow 1$ **to** n **do**
  for $i \leftarrow 1$ **to** l **do**
    $I_{i,j} \leftarrow \{k \mid (\tilde{c}[k, j] - \tilde{c}_{\mathrm{rl}}[i])^2 \leq \epsilon_{\mathrm{tol}}\}$;
    if $I_{i,j} = \emptyset$ **then**
      $\tilde{\rho}[i, j] \leftarrow 0.0$;
    else
      $\tilde{\rho}[i, j] \leftarrow \frac{\sum_{k \in I_{i,j}} \tilde{r}[k]^3}{4/3\pi}$;
return $\tilde{\rho}$

To convert the population density to XRD intensity, we assume a peak shape function $\mathcal{P}$ for particles of concentration

$\tilde{c}$ centered around $\theta_0(\tilde{c})$ in the form of

$$\mathcal{P}(\theta;\tilde{c}) = C\exp\left(-4\ln 2\left(\frac{2\theta - 2\theta_0(\tilde{c})}{H}\right)^2\right),$$

where θ is the diffraction angle. The parameters C and H are tuning constants dependent on the instrumentation and setup. The function $\theta_0(\tilde{c})$ for graphite is fitted to the experimental results [17], and the tuning parameters are fitted using XRD data [17] to each model separately. The XRD intensity $\mathcal{I}$ is calculated by an integral

$$\mathcal{I}(\theta,t) = \int_0^1 \rho(\tilde{c},t)\mathcal{P}(\theta;\tilde{c})d\tilde{c}.$$

S7. Physical parameters

Nomenclature

Table 1: Nomenclature, assigned values and meanings of the symbols used in this study.

Constant	Value	Meaning
e_0	1.602×10^{-19}	elementary charge [C]
N_A	6.022×10^{23}	Avogadro's number [mol^{-1}]
k_0	fitted	reaction rate constant [$\mathrm{m}^{-2}\mathrm{s}^{-1}$]
D_0	fitted	Diffusion coefficient [$\mathrm{m}^{-2}\mathrm{s}^{-1}$]
$C_{\max}$	fitted	maximum lithium site density [m^{-3}]
κ	fitted	gradient energy coefficient [eV]
a_s	fitted	specific interfacial surface area [m^{-1}]
ϵ_s	fitted	volume fraction of active material
V_p	fitted	total active particle volume [m^3]
N_p	fitted	number of total active particles
R	fitted	particle radius [m]
C_e	fitted	electrolyte steady-state concentration [$\mathrm{mol}\cdot\mathrm{m}^{-3}$]
$\mathcal{F}$	96487	Faraday constant [$\mathrm{C}\cdot\ \mathrm{mol}^{-1}$]
k_B	1.38×10^{-23}	Boltzmann constant [$\mathrm{m}^2\cdot\mathrm{kg}\cdot\mathrm{s}^{-2}\cdot\mathrm{K}^{-1}$]
Q_n	7.5	nominal capacity [Ah]
A_s	fitted	electrode active surface area [m^2]
$\tilde{\lambda}$	5	Marcus reorganization energy scaled to k_BT
i_0	fitted	intercalation rate constant [$\mathrm{m}^{-2}\mathrm{s}^{-1}$]
ν	fitted	thermal diffusivity [s^{-1}]
ϕ_{ref}	0.18	reference potential [V]

OCP function for the PET-based model

To parameterize the anode potential model derived from porous electrode theory (PET) with an output equation (19), we employ an empirical nonlinear function denoted by $\phi_{\mathrm{OCP}}(C_s^R)$. This is the most frequently used OCP fitting function

in pseudo-two-dimensional battery models [18].

$$
\begin{aligned}
x_{\mathrm{a}} &= \frac{C_s^R}{C_{\max}} \times A - B, \\
\phi_{\mathrm{OCP}} &= 0.1493 + 0.8493 \exp\left(-61.79 x_{\mathrm{a}}\right) + 0.3824 \exp\left(-665.8 x_{\mathrm{a}}\right) - \\
&\quad \exp\left(39.42 x_{\mathrm{a}} - 41.92\right) - 0.03131 \operatorname{atan}(25.59 x_{\mathrm{a}} - 4.099) - \\
&\quad 0.009434 \operatorname{atan}(32.49 x_{\mathrm{a}} - 15.74).
\end{aligned}
$$

Here, x_{a} represents the anode stoichiometry. We introduce fitted scaling factors $A = 1.2343$ and $B = 0.0893$ to scale the dimensionless concentration $C_s^R / C_{\max}$. This scaling aligns the modeled half-cell anode potential with experimental measurements. Our rationale for this adjustment stems from the fixed initial stoichiometries for charge and discharge in our models. Rather than following the conventional practice of fitting initial stoichiometries, as often seen in the literature [19], we opt to scale the dimensionless concentration. Importantly, it can be demonstrated that these two approaches yield equivalent results.

Parameter distribution

The posteriors of the physical parameters of these battery models are of particular interest in parameter identification. A common issue in fitting the parameters to experimental data is that some parameter combinations yield nearly identical model outputs given the same excitation signal. For example, parameters in the DFN model are known for their poor inferability, with many parameters remaining non-identifiable under constant current discharge, leading to infinite confidence intervals of probability densities [20]. To accurately capture the posterior distribution of physical parameters, we performed an approximate Bayesian computation based on sequential Monte Carlo [21] using the parameter distributions obtained from the sampling phase of SGLD as priors. Since the raw samples from the posterior can be noisy and sparse in high-dimensional spaces, we employed kernel density estimation (KDE) to approximate the continuous probability density functions of these parameters.

KDE is a non-parametric method that constructs a smooth estimate of the underlying distribution by convolving each sample point with a kernel function. Specifically, we applied Gaussian kernels, which are widely recognized for their ability to balance smoothness and local detail in probability density approximations. The bandwidth of the kernel, a crucial hyperparameter, was optimized to ensure that the KDE sufficiently captures the distribution shape without over-smoothing or introducing artifacts.

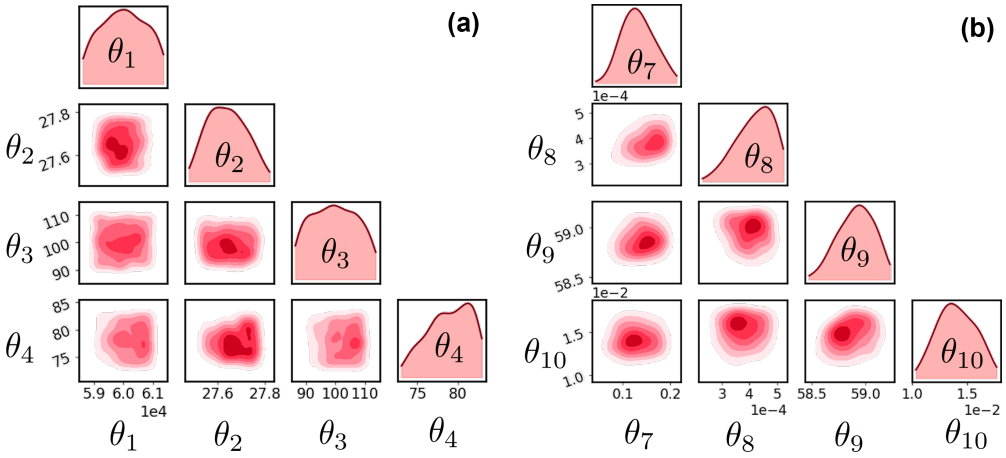

Figure 5: (a) Correlation plot of the physical parameters of the phase-field model. Only four parameters are shown here for simplicity. (b) Correlation plot of the physical parameters of the reaction-limited model.

These parameters are grouped and defined in Section S.4. Fig. 5a and 5b show the correlation plots of the physical parameters for the phase-field and reaction-limited models, respectively. The resulting posterior distributions contain sufficient information to uniquely identify these grouped parameters. This is demonstrated by the finite confidence intervals of the parameter probability densities shown along the diagonals of Fig. 5a and 5b. From a practical perspective, this indicates that even a simple half-cell charge-discharge experiment can provide adequate information for parameterizing the models effectively, enabling their use in real-world applications.

S8. Synthetic data and benchmark

While real-world applications often involve unknown uncertainties in both measurement and unmodeled dynamics, the process of generating synthetic data allows us to control the true parameter values explicitly and observe how accurately they are inferred under different noise settings and models. In this benchmark, we evaluate the performance of BMINN and inverse physics-informed neural networks (iPINN) in learning the Gibbs free energy for lithium iron phosphate (LFP) material, which has a well-established form for its Gibbs free energy. The Gibbs free energy is defined as:

$$\mathcal{G}_{\text{LFP}} = \hat{c}\log(\hat{c}) + (1-\hat{c})\log(1-\hat{c}) + \Omega(\hat{c}-\hat{c}^2), \tag{22}$$

where $\hat{c}$ represents the normalized concentration of lithium ions, the first term accounts for the configurational entropy of lithium sites, the second term accounts for vacancies, and Ω is the interaction parameter controlling phase separation. LFP is particularly suitable for benchmarking because its Gibbs free energy is analytically known, making it possible to quantify the accuracy of inferred parameters and potentials.

For this benchmark, we consider four different levels of noise (0, 1, 5, and 10) of commercially available sensors [22] and added them respectively to the synthetic voltage data for training. The results, shown in Table 2, compare the performance of BMINN and iPINN in recovering the true underlying parameters and chemical potentials across these noise levels. The physics-based models presented in this work involve highly nonlinear terms. Specifically, the reaction-limited model features a convection-dominated system with variable flux, constrained by a nonlinear algebraic equation. This PDAE formulation cannot be effectively learned by physics-informed neural networks. When the algebraic component is incorporated as a soft constraint, the resulting PDE system produces an ill-conditioned residual term, making it susceptible to gradient pathologies.

Through extensive experimentation, we observed that applying inverse PINN to new problems remains challenging. Despite significant advancements in the five years since PINN were introduced and three decades of research on using differentiable neural networks to solve differential equations [23], there is still no straightforward, plug-and-play version of PINN that can be seamlessly adapted to diverse problem types, such as the ones encountered in this work. To this end, we modified PINN and tailored it to our problem using adaptive loss balancing [24]. In this benchmark, iPINN's implementation is limited by its reliance on learning a single parameter, Ω, with the ground truth set to $\Omega = 2.5$. As shown in the iPINN column of Table 2, even with this simplification, iPINN is unable to accurately infer the underlying chemical potential when noise is present.

As shown in Table 2, the learned μ/k_BT for iPINN diverges significantly from the ground truth under all noise levels except zero. Furthermore, iPINN struggles to converge efficiently, requiring a large number of epochs for training and still failing to capture the underlying dynamics under higher noise levels. BMINN consistently outperforms iPINN across all noise levels, with significantly lower Mean Absolute Errors (MAE) in inferred chemical potentials and more robust parameter recovery. For instance, at noise level 1, BMINN achieves an MAE of 9.79×10^{-3}, compared to iPINN's error exceeding 10^2. These results are attributed to BMINN's physics-based constraints, which directly embed thermodynamic equations into the learning process. This embedding limits the solution space and accelerates convergence, with the loss stabilizing after approximately 100 epochs across all noise levels.

One of the key advantages of BMINN is its ability to directly learn the chemical potential, μ/k_BT, with high accuracy,

Noise Level	BMINN	iPINN
0	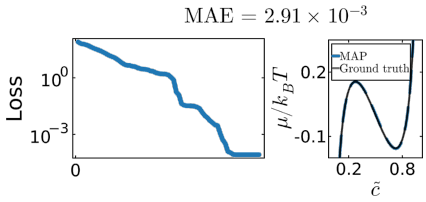	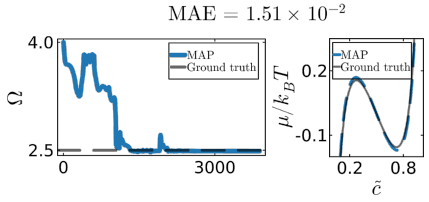
1	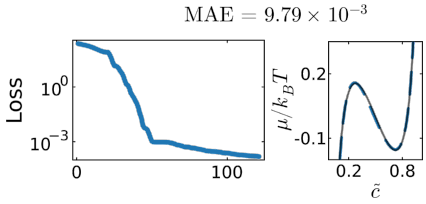	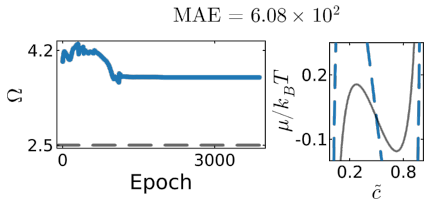
5	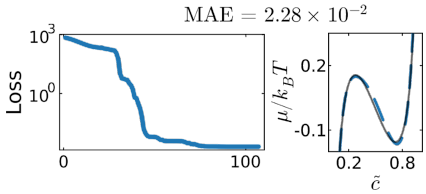	
10	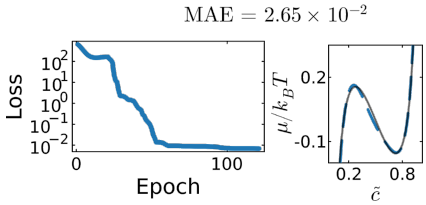	

Table 2: Benchmark results for BMINN and iPINN under different noise levels. The plots compare the loss, learned chemical potential, and MAE for both methods. BMINN consistently outperforms iPINN in terms of accuracy and efficiency, whereas iPINN fails to perform reliably even at noise level 1.

even under noisy conditions. The thermodynamically consistent potentials learned by BMINN align closely with the ground truth, as illustrated in Table 2. In contrast, iPINN's learned potentials deviate significantly, highlighting its inability to handle noise and capture the underlying physics. Another critical observation is BMINN's training efficiency. The loss for BMINN rapidly decreases and stabilizes after approximately 100 epochs, as shown in Table 2. This efficiency is achieved because BMINN constrains the learning process using built-in physics-based equations, reducing the search space for solutions. Conversely, iPINN requires thousands of epochs but still struggles to achieve comparable accuracy.

Further, we highlight that BMINN successfully recovers the true parameter values and provides a probabilistic assessment. In Table 3, the confidence intervals (CI) appropriately adapt to the noise level, widening in higher noise scenarios that reflect increased uncertainty. The finite CI indicates a unimodal distribution and identifiable parameters, confirming the robustness of the BMINN model even under challenging conditions. Specifically, as the noise level increases, the CIs expand while still centering around the true values, demonstrating the model's ability to quantify uncertainty effectively and maintain consistency with the underlying physics.

	Noise Level 0	Noise Level 10
Data	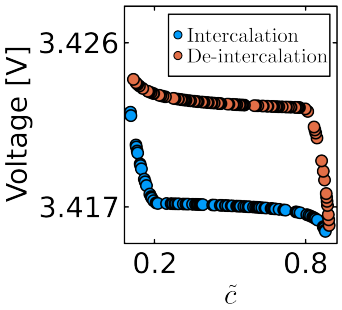	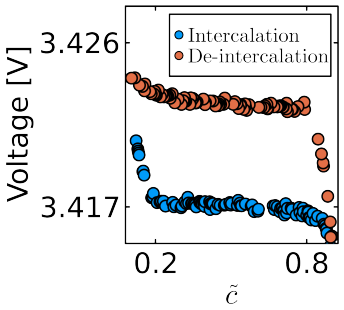
Chemical Potential	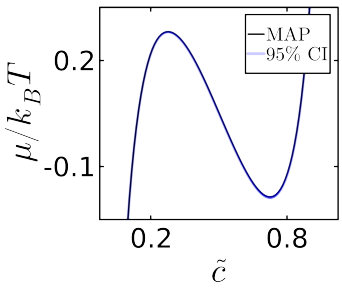	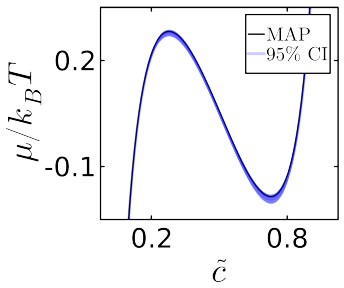
Gibbs Free Energy	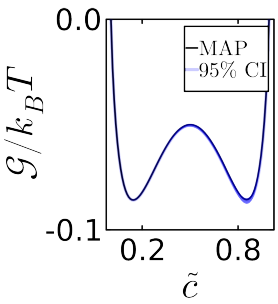	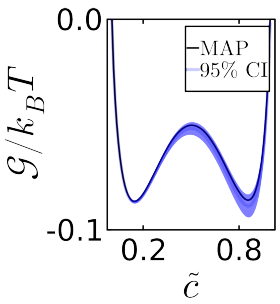

Table 3: Performance of BMINN under noise levels 0 and 10. The table illustrates the observed (synthetic) data used for learning, learned chemical potential, and Gibbs free energy along with their 95% confidence intervals (CI).

S9. BMINN training

This section describes the BMINN training workflow shown in Algorithm 2, corresponding to the schematic in Fig. 6f. The goal of training is to infer (i) the parameters of the Bayesian neural network (BNN) that represents the hidden physics and (ii) a reduced set of identifiable physical parameters, using only measured input–output data while enforcing the physics-based PDAE model during forward simulation.

Algorithm 2: BMINN training

Input: Measured data $\mathcal{D}_{\text{full}} = \{(u(t_i), \hat{y}(t_i))\}_{i=1}^{N}$
Physics-based recurrent unit (Eqs. (4a)–(4b)) and solver $\mathcal{S}$
Initial hidden states (h^0, z^0)
Mini-batch length K, max iterations $\tau_{\max}$, step-size schedule $\{\epsilon_\tau\}$
Output: Posterior samples $\{\theta_\tau\}$ and MAP estimate θ_{MAP}
Initialize parameters θ_0
for $\tau \leftarrow 0$ **to** $\tau_{\max} - 1$ **do**
  Select random mini-batch $\mathcal{D}_\tau = \{(u^k, \hat{y}^k)\}_{k=0}^{K-1}$ from $\mathcal{D}_{\text{full}}$
  Set (h^0, z^0) for this mini-batch
  for $k \leftarrow 0$ **to** $K - 1$ **do**
    $\Phi^k \leftarrow \Phi_{\text{BNN}}(k, \mathbf{x}, h^k, z^k, u^k; \theta_\tau)$
    $(h^{k+1}, z^{k+1}) \leftarrow \mathcal{S}\big(h^k, z^k, u^k, \Phi^k, \theta_\tau\big)$
    $y^k \leftarrow Y(h^k, z^k, u^k, \theta_\tau)$
  $\mathcal{L}_{\text{BMINN}}(\theta_\tau) \leftarrow \frac{1}{K}\sum_{k=0}^{K-1}(y^k - \hat{y}^k)^2$
  $G_\tau \leftarrow \nabla_\theta \mathcal{L}_{\text{BMINN}}(\theta_\tau)$
  Sample $\eta_\tau \sim \mathcal{N}(0, I)$
  $\theta_{\tau+1} \leftarrow \theta_\tau - \frac{\epsilon_\tau}{2} G_\tau + \sqrt{\epsilon_\tau}\,\eta_\tau$
Estimate $p(\theta|\mathcal{D}_{\text{full}})$ from $\{\theta_\tau\}$ and compute θ_{MAP}

References

[1] H. Fujimoto, T. Yamaki, K. Shimoda, S. Fujinami, T. Nakatani, G. Kano, M. Kawasaki, Z. Ogumi, T. Abe, Phase diagram of li-graphite intercalation compound formed by the charge/discharge reaction in li-ion battery, Journal of The Electrochemical Society 169 (7) (2022) 070507.

[2] T. F. Fuller, M. L. Doyle, J. Newman, Simulation and optimization of the dual lithium ion insertion cell, Journal of The Electrochemical Society 141 (1994) 1–10.

[3] S. Hess, A. Latz, S. Thiele, J. Zausch, J. Eller, H. D"oring, F. Holzer, I. Manke, V. Schmidt, A. Weber, In situ observation and mathematical modeling of lithium distribution within graphite, Journal of The Electrochemical Society 164 (11) (2017) E3063–E3072. doi:10.1149/2.0061711jes.

[4] T. Gao, D. A. Cogswell, M. Z. Bazant, Interplay of lithium intercalation and plating on a single graphite particle, Joule 5 (2) (2021) 393–414. doi:10.1016/j.joule.2020.12.020.

[5] S. Lian, Q. Xu, J. Li, Z. Deng, Y. Yu, K.-H. Chen, Modeling lithium plating onset on porous graphite electrodes, Journal of The Electrochemical Society 171 (1) (2024) 010526. doi:10.1149/1945-7111/ad1e3d.

[6] R. B. Smith, M. Z. Bazant, Multiphase porous electrode theory, Journal of The Electrochemical Society 164 (11) (2017) E3291.

[7] J. Newman, K. Thomas-Alyea, Electrochemical Systems, The ECS Series of Texts and Monographs, Wiley, 2004.

[8] A. Van der Ven, S. Auerbach, K. Smith, Hysteresis in electrochemical systems, Battery Energy 1 (2) (2022) e20210017. doi:10.1002/bte2.20210017.

[9] X. Lu, D. P. Finegan, J. L. Fife, H. Wang, S. Zhang, K. Dai, M. Di Michiel, S. Checcia, K. Smith, D. J. L. Brett, P. R. Shearing, M. Z. Bazant, Multiscale dynamics of charging and plating in graphite electrodes coupling operando microscopy and phase-field modelling, Nature Communications 14 (1) (2023) 5127. doi:10.1038/s41467-023-40574-6.

[10] W. Dreyer, C. Guhlke, R. Huth, The behavior of a many-particle electrode in a lithium-ion battery, Physica D: Nonlinear Phenomena 240 (2011) 1008–1019.

[11] H. Zhao, M. Z. Bazant, Population dynamics of driven autocatalytic reactive mixtures, Physical Review E 100 (2019) 012144.

[12] D. Fraggedakis, M. McEldrew, R. B. Smith, Y. Krishnan, Y. Zhang, P. Bai, W. C. Chueh, S. Yang, M. Z. Bazant, Theory of coupled ion-electron transfer kinetics, Electrochimica Acta (2020).

[13] C. R. Birkl, M. R. Roberts, E. McTurk, P. G. Bruce, D. A. Howey, Degradation diagnostics for lithium ion cells, Journal of Power Sources 341 (2017) 373–386.

[14] P. Oßwald, S. V. Erhard, J. Wilhelm, H. E. Hoster, A. Jossen, Simulation and measurement of local potentials of modified commercial cylindrical cells: I. cell preparation and measurements, Journal of The Electrochemical Society 162 (2015).

[15] F. Oehler, A. Graule, S. Kücher, T. Roth, A. Adam, J. Li, E. Ronge, R. Mörtel, A. Jossen, Multi-reference electrode lithium-ion pouch cell design for spatially resolved half-cell potential and impedance measurements, Journal of The Electrochemical Society (2023).

[16] D. Monasterial, D. Tang, S. Gopalakrishnan, M. Landstorfer, U. Aydemir, W. Tremel, J. Martin, Dynamic in-plane heterogeneous and inverted response of lithium-ion battery anodes during electrochemical insertion, Small Science 3 (7) (2023) 2200067. doi:10.1002/smsc.202200067.

[17] C. Schmitt, A. Kube, N. Wagner, C. Friedrich, Understanding the influence of temperature on phase evolution in graphite during charge and discharge: An operando x-ray diffraction study, ChemElectroChem 9 (2) (2022) e202101342. doi:10.1002/celc.202101342.
[18] K.-H. Chen, F. Planella, K. O'Regan, D. Gastol, W. D. Widanage, E. Kendrick, Development of experimental techniques for parameterization of multi-scale lithium-ion battery models, Journal of The Electrochemical Society 167 (8) (2020) 080534. doi:10.1149/1945-7111/ab9050.
[19] E. Namor, D. Torregrossa, R. Cherkaoui, M. Paolone, Parameter identification of a lithium-ion cell single-particle model through non-invasive testing, Journal of energy storage 12 (2017) 138–148.
[20] M. D. Berliner, H. Zhao, S. Das, M. Forsuelo, B. Jiang, W. H. Chueh, M. Z. Bazant, R. D. Braatz, Nonlinear identifiability analysis of the porous electrode theory model of lithium-ion batteries, Journal of The Electrochemical Society (2021).
[21] T. Toni, D. Welch, N. Strelkowa, A. Ipsen, M. P. H. Stumpf, Approximate Bayesian computation scheme for parameter inference and model selection in dynamical systems, Journal of The Royal Society Interface 6 (2009) 187–202.
[22] Y. Zhang, T. Wik, J. Bergstr"om, C. Zou, Machine learning-based lifelong estimation of lithium plating potential: A path to health-aware fastest battery charging, Energy Storage Materials 74 (2025) 103877. doi:10.1016/j.ensm.2024.103877.
[23] H. Lee, I. S. Kang, Neural algorithm for solving differential equations, Journal of Computational Physics 91 (1) (1990) 110–131.
[24] S. Wang, Y. Teng, P. Perdikaris, Understanding and mitigating gradient flow pathologies in physics-informed neural networks, SIAM Journal on Scientific Computing 43 (5) (2021) A3055–A3081.